

Line source representation for laser-generated ultrasound in an elastic transversely isotropic half-space

David H. Hurley

Physics Group, Idaho National Engineering and Environmental Laboratory, Idaho Falls, Idaho 83415-2209

James B. Spicer

Department of Materials Science and Engineering, The Johns Hopkins University, Baltimore, Maryland 21218

(Received 14 February 2004; revised 16 July 2004; accepted 18 July 2004)

Theoretical and experimental results are presented for a laser line source in an elastic, transversely isotropic half-space. The thermoelastic source (laser source) is represented as an appropriately weighted shear stress dipole applied at the sample surface. The plane of isotropy coincides with the half-space boundary. Analytical expressions representing the out-of-plane displacements for the surface wave and for the epicentral cases are given for all crystal classes that exhibit elastic transverse isotropy. In addition, quasianalytical results are given for observation points off the epicentral axis. Theoretical wave forms for all of the source/observation geometries considered are compared with experimental wave forms generated in single crystal zinc samples. The close comparison between experiment and theory confirms, for this particular line source orientation and crystal symmetry, that a laser line source is accurately modeled using an equivalent boundary stress. © 2004 Acoustical Society of America. [DOI: 10.1121/1.1791721]

PACS numbers: 43.35-Sx, 43.20.Bi, 43.35.Zc [YHB]

Pages: 2914–2922

I. INTRODUCTION

Since the early 1980s, laser generated ultrasound has been used to determine material properties and to characterize material defects^{1–3} To a large extent, the success of laser ultrasonics has been the researcher's ability to correctly predict the temporal evolution of the displacement wave form resulting from pulsed laser irradiation. Theories that assume isotropic elastic properties work well for crystalline materials that have randomly oriented grains which are small compared to the wavelength of the interrogating ultrasonic wave.⁴ However, for single crystals, the anisotropic nature of the material must be considered.⁵

Stoneley,⁶ studied the propagation of Rayleigh surface waves in certain single crystal systems. In particular, Stoneley analyzed three specific cases, surface waves propagating in the (0 0 1) plane of cubic crystals along the [1 0 0] and [1 1 0] directions, and in the basal plane of hexagonal crystals. Royer and Dieulesaint⁷ extended the work of Stoneley to include the analysis of Rayleigh wave propagation in orthorhombic and tetragonal systems. The analysis by Stoneley⁶ and Royer and Dieulesaint⁷ considered the disturbance to have a planar phase front.

To gain a better understanding of the underlying physics, the finite extent of the source must also be considered. Kraut⁸ extended the work of Lamb⁹ by considering a transversely isotropic elastic half-space subjected to a source of finite extent. Kraut used the method of Cagniard-de Hoop^{10,11} to study the resulting displacements in single crystal Beryl. Other researchers^{12–15} have extended the work by Kraut.⁸ For instance, Mourad *et al.*¹⁴ used the Cagniard-de Hoop method to numerically obtain the solutions to Lamb's problem in an anisotropic half-space. In their paper, Mourad *et al.* assumed that the laser source could be modeled as a shear stress dipole^{16–18} applied at the bounding surface. Of particu-

lar interest to this paper is the work by Payton¹⁹ who has treated a general class of problems for crystals that exhibit transverse isotropy. Payton furnished a detailed analysis of the solution and the solution technique for a variety of transient problems in bounded and unbounded solids. In addition, Payton gave an explicit set of conditions, related to the elastic parameters of the material, that predict the existence of inflection points on the slowness curve. It is well known^{5,8,19,20} that these inflection points lead to behavior in anisotropic materials that is markedly different from that in isotropic materials. Thus, while transverse isotropy is perhaps the simplest case to treat, it nonetheless exemplifies the peculiar behavior found in elastically anisotropic materials.

In this paper, the homogeneous equations of motion for a transversely isotropic material are solved subjected to a set of stress boundary conditions which has been shown to be equivalent to a thermoelastic line source in the limit of strong optical absorption.¹⁸ The plane of isotropy coincides with the boundary plane and the epicentral direction coincides with the crystal symmetry axis and the x_3 axis, Fig. 1. For this problem geometry/crystal symmetry, the source specification and the solution are independent of the line source orientation.¹⁸ However, for convenience the line source is taken to coincide with the x_1 axis. Expressions representing the out-of-plane displacements for wave propagation along (1) the free surface, (2) epicentral axis, and (3) off the epicentral axis are given. In all cases the solutions are sought using the method of Cagniard-de Hoop. The first two cases lend themselves to analytic solutions which in turn affords a detailed analysis of the solution procedure. The last case is solved using a quasianalytical approach in which the integration contour must be defined numerically. It is shown that for the epicentral and off epicentral cases, the form of the solution depends strongly on the nature of the material anisotropy. For the sake of comparison with experimental

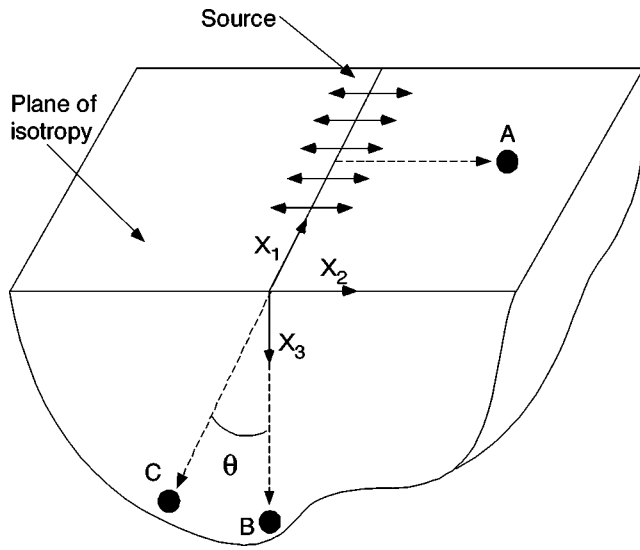


FIG. 1. Problem geometry with source location and observation points (A,B,C). The line source is parallel to the x_1 axis and the sample normal is parallel with the x_3 axis and the crystal symmetry axis.

results, particular attention will be paid to zinc. Theoretical results are compared with experimental wave forms in a sample of single crystal zinc. Owing to the transversely isotropic nature of the problem, the development of a line source solution closely parallels the development of the more general point source solution of Hurley and Spicer.^{21,22}

II. THEORY

Before embarking on a solution procedure, it is convenient to classify transversely isotropic crystals according to the behavior of the displacements of these crystals along the symmetry axis. Borrowing notation from Payton,¹⁹ these categories are

- (i) $(\alpha + \beta) < \gamma < (1 + \alpha\beta)$,
- (ii) $(\beta + 1) < \gamma < (\alpha + \beta)$ and $(\gamma^2 - 4\alpha\beta) < 0$,
- (iii) $\gamma < (\beta + 1)$ and $(\gamma^2 - 4\alpha\beta) < 0$ also $\beta > \alpha$,

where the ratios of the elastic stiffness components, α , β , γ and κ are defined as

$$\alpha = \frac{c_{33}}{c_{44}}, \quad \beta = \frac{c_{11}}{c_{44}}, \quad \kappa = (1 + \alpha\beta - \gamma)^{1/2},$$

$$\gamma = 1 + \alpha\beta - \left(\frac{c_{13}}{c_{44}} + 1 \right)^2. \quad (2)$$

For crystals belonging to the first category in Eq. (1), the roots of the slowness equation are purely imaginary. In addition, there are no cusps in the wave-front curves that intersect the symmetry axis for class (i) crystals. The crystals belonging to categories (ii) and (iii) have complex roots. For class (iii) crystals, the triangular portion of the wave-front (lacuna) is centered on the symmetry axis. It will be shown that for class (i) crystals, the solutions along the free surface and along the epicentral direction behave in a similar manner to isotropic materials. However, the solution for class (ii) and

(iii) crystals along the symmetry axis and off the symmetry axis differs profoundly from their isotropic counterpart.

For transversely isotropic materials with the plane of isotropy coinciding with the bounding plane, the equivalent stress boundary conditions are independent of line source orientation¹⁸ and are given as

$$(\sigma_{23})|_{x_3=0} = \tilde{F} \delta'(x_2) H(\tau), \quad (\sigma_{33})|_{x_3=0} = 0,$$

$$\tilde{F} = (F_3(1 - \kappa) + F_2\alpha), \quad F_2 = \frac{B_{22}T_0}{\alpha}, \quad F_3 = \frac{B_{33}T_0}{\alpha}, \quad (3)$$

where $T_0 = q_0 / \rho C$ (Refs. 17, 23, and 24) is the instantaneous temperature rise and B_{ij} are the thermal pressure coefficients. The time coordinate, $\tau = \sqrt{(C_{44}/\rho)}t$, which has dimensions of length, was introduced so that the current analysis is consistent with that of Payton.¹⁹ The transformed homogenous equations of motion appropriate for a line source applied along a plane of transverse isotropy are given by

$$-\beta \eta^2 \bar{u}_2 + \bar{u}_{2,33} - s^2 \bar{u}_2 + i\kappa \eta \bar{u}_{3,3} = 0,$$

$$i\eta \kappa \bar{u}_{2,3} - \eta^2 \bar{u}_3 + \alpha \bar{u}_{3,33} - s^2 \bar{u}_3 = 0. \quad (4)$$

where s and η are the transform parameters for t and x_2 , respectively.²⁵ Solutions to the above system of equations are of the form

$$\bar{u}_2(\eta, x_3, s) = A_1 e^{-k_1 x_3} + A_2 e^{-k_3 x_3},$$

$$\bar{u}_3(\eta, x_3, s) = A_3 e^{-k_1 x_3} + A_4 e^{-k_3 x_3}, \quad (5)$$

where $k_{1/3}$ are the physical roots to the slowness curve. Next, the following substitution will be made so as to facilitate the Cagniard inversion technique:

$$k = s\zeta, \quad \eta = s\omega. \quad (6)$$

The denominator of the secular equation can be rewritten using the above substitutions as

$$\alpha \zeta^4 - \zeta^2((\alpha + 1) + \gamma \omega^2) + (\beta \omega^4 + (\beta + 1)\omega^2 + 1) = 0. \quad (7)$$

The four roots to Eq. (7) may be written as

$$\zeta_1(\omega) = \frac{[(\alpha + 1) + \gamma \omega^2 + \sqrt{\phi(\omega)}]^{1/2}}{\sqrt{2\alpha}},$$

$$\zeta_2(\omega) = -\zeta_1(\omega),$$

$$\zeta_3(\omega) = \frac{[(\alpha + 1) + \gamma \omega^2 - \sqrt{\phi(\omega)}]^{1/2}}{\sqrt{2\alpha}},$$

$$\zeta_4(\omega) = -\zeta_3(\omega),$$

$$\phi(\omega) = [\gamma \omega^2 + (\alpha + 1)]^2 - 4\alpha[\beta \omega^4 + (\beta + 1)\omega^2 + 1]. \quad (8)$$

The coefficients A_3 and A_4 are related to A_1 and A_2 by the fact that the above displacements must solve the equations of motion. By substituting both solutions into the transformed equations of motion, it can be shown that

$$A_1 = A_3 \left[\frac{\alpha \zeta_1^2 - \omega^2 - 1}{i\kappa \omega \zeta_1} \right], \quad (9)$$

$$A_2 = A_4 \left[\frac{\alpha \zeta_3^2 - \omega^2 - 1}{i \kappa \omega \zeta_3} \right].$$

The coefficients $A_{3/4}$ are found by requiring the displacements in Eq. (5) satisfy the boundary conditions in Eq. (3),

$$\begin{aligned} A_3 &= \frac{\tilde{F} \zeta_1 \omega^2}{s C_{44} (\zeta_1 - \zeta_3) D} [\alpha \zeta_3^2 + (\kappa - 1) \omega^2 + (\kappa - 1)], \\ A_4 &= \frac{-\tilde{F} \zeta_3 \omega^2}{s C_{44} (\zeta_1 - \zeta_3) D} [\alpha \zeta_1^2 + (\kappa - 1) \omega^2 + (\kappa - 1)], \quad (10) \\ D &= [2(1 - \kappa)(\omega^4 + \omega^2) - (\gamma \omega^2 + \alpha)(\omega^2 + 1) - \alpha \zeta_1 \zeta_3], \end{aligned}$$

where D is the Rayleigh denominator.

A. Solutions along the bounding surface

For displacements along the bounding plane ($x_3 = 0$), the Cagniard integration path is along the imaginary ω axis. Operating on the u_3 displacement with the inverse Fourier operator as follows, and noting that u_3 is even in ω , gives

$$\begin{aligned} \bar{u}_3(x_2, 0, s) &= \text{Re} \frac{1}{\pi} \int_0^\infty \tilde{u}_3(s, \omega) d\omega, \\ \tilde{u}_3(s, \omega) &= \frac{-\tilde{F} \omega^2}{C_{44} D} [\alpha \zeta_1 \zeta_3 + (1 - \kappa)(\omega^2 + 1)] e^{i s \omega |x_2|}, \quad (11) \end{aligned}$$

Cagniard Path $\rightarrow i\omega|x_2| = \tau = \text{real}$.

Before the Cagniard inversion can be performed, the branch points and singularities associated with \bar{u}_3 must be identified. Branch points for $\xi(\omega)$ may arise in two distinct ways:

- (i) $\phi(\omega) = 0$,
- (ii) $\gamma \omega^2 + (\alpha + 1) \pm \sqrt{\phi(\omega)} = 0$. (12)

Presently, only the inversion of u_3 is being considered. Since u_3 is an even function of $\sqrt{\phi(\omega)}$, branch points arising from (i) in Eq. (12) need not be considered. The singularities in the function $D(\omega)$ will now be discussed. Since the branch points for this function have been discussed above, only pole singularities in $D(\omega)$ need to be considered. After squaring and simplifying, the equation for the Rayleigh denominator yields

$$\begin{aligned} a^6 \omega^2 + a(a + 2\alpha) \omega^4 + \alpha(2a + \alpha - \beta) \omega^2 + \alpha(\alpha - 1) &= 0, \\ a &= 2\kappa - 2 + \gamma. \end{aligned} \quad (13)$$

The roots of interest will lie on the positive imaginary axis. The remaining roots will lie on the nonphysical sheets of the Riemann surface. The (Rayleigh) pole of Eq. (13) will be denoted by $D(i\omega_r) = 0$. Now the integration contour and the subsequent inversion of the integral in Eq. (11) may be performed. Figure 2 shows the complex ω plane along with the integration contour. The real axis coincides with the Fourier inversion path and the imaginary axis coincides with the Cagniard inversion path. The inverted solution may be written formally as

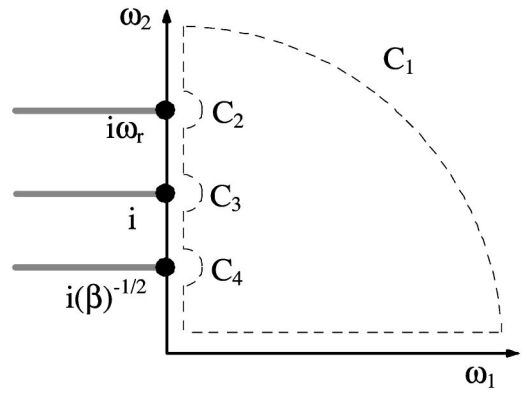


FIG. 2. Integration contour for the vertical displacement, u_3 , at the bounding surface.

$$\begin{aligned} u_3(x_2, 0, \tau) &= L^{-1} \left[\frac{1}{\pi} \text{Re} \left\{ \int_{C_1} + P \int_{\infty}^1 \tilde{u}_3(s, i\omega_2) i d\omega \right. \right. \\ &\quad + \{i \pi \text{residue@} \omega = i\omega_r\} \\ &\quad + \int_{C_3} + \int_1^{1/\sqrt{\beta}} \tilde{u}_3(s, i\omega_2) i d\omega \\ &\quad \left. \left. + \int_{C_4} + \int_{1/\sqrt{\beta}}^0 \tilde{u}_3(s, i\omega_2) i d\omega \right\} \right], \quad (14) \end{aligned}$$

where L^{-1} is the inverse Laplace operator and the P in front of the second integral denotes the Cauchy principle value. A typical displacement wave form generated using Eq. (14) is shown in the inset of Fig. 3. The initial disturbance, referred to as the surface-skimming bulk wave, arrives at the longitudinal velocity and vanishes at the shear wave velocity. The later arriving Rayleigh wave travels as a Dirac delta function. The characteristics of the wave form for class (i), class (ii),

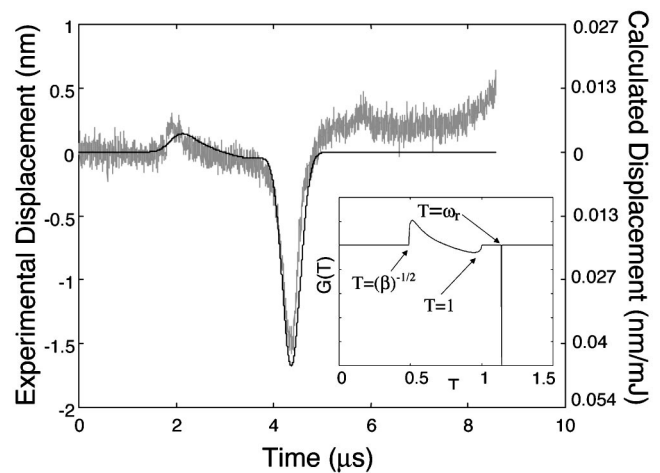


FIG. 3. Comparison between experiment and theory for the surface wave case. The sample is single crystal zinc with the c axis perpendicular to the free surface. The nonzero experimental displacement corresponding to the interval between the end of the surface skimming bulk wave and the arrival of the Rayleigh pulse is a result of pulse broadening. Inset: Theoretical displacement, u_3 , for surface waves generated with a line source in zinc as a function of $T = \tau/x_2$. A delta function is represented by vertical line at $T = 1.13$.

and class (iii) materials are similar. The similarity is due to the fact that the contribution from the branch point corresponding to (i) in Eq. (12) does not affect the solution for the vertical displacement. However, this is not the case for the in-plane displacement components.

B. Solutions along the symmetry axis

Another class of solutions that can be inverted easily using the Cagniard technique corresponds to solutions along the epicentral axis, or for this particular experimental geometry, along the symmetry axis [see observation point (B) in Fig. 1]. The location of the Cagniard path in the complex plane depends on the category of crystal being investigated. For materials belonging to category (i), the Cagniard path is along the real ω axis. For class (ii) and (iii) materials, the Cagniard path is off the real ω axis. The formal solution for the out-of-plane displacement along the epicentral axis is given as

$$\begin{aligned}\bar{u}_3(0, x_3, s) &= \frac{1}{2\pi} \int_{-\infty}^{\infty} \tilde{u}_3(\eta, x_3, s) s d\omega, \\ \tilde{u}_3(\eta, x_3, s) &= A_3 e^{-\xi_1 x_3 s} + A_4 e^{-\xi_3 x_3 s},\end{aligned}\quad (15)$$

where A_3 and A_4 are defined in Eq. (10). Also note that since the roots to the slowness equations, ξ_1 and ξ_3 , are even functions of ω , $\tilde{u}_3(\eta, x_3, s)$ is also even, allowing the integration limit to be changed to the positive ω axis. For convenience the following substitutions are made:

$$\begin{aligned}\varpi &= \omega^2, \\ \bar{u}_3(0, x_3, s) &= \frac{1}{\pi} \text{Re}\{I_1 + I_3\}, \\ I_1 &= \int_0^{\infty} \bar{A}_3 e^{-\xi_1 x_3 s} d\varpi, \quad I_3 = \int_0^{\infty} \bar{A}_4 e^{-\xi_3 x_3 s} d\varpi, \\ \bar{A}_{3/4} &= \frac{A_{3/4} s}{2\sqrt{\varpi}}.\end{aligned}\quad (16)$$

This substitution consolidates the branch cuts along the real and imaginary axes so they both lie on the real axis. The Cagniard path for the integrals in Eq. (16) is defined by

$$\begin{aligned}\xi_{1/3}(\varpi) x_3 &= \tau, \\ \tau &\text{ is real and positive.}\end{aligned}\quad (17)$$

1. Solution for class (i) materials

For class (i) materials, the above condition on τ is met for real ϖ , giving the positive real ϖ axis as the Cagniard contour. Solving Eq. (8) for ϖ in terms of τ gives

$$\begin{aligned}\varpi_{1/3} &= \frac{-B \pm \sqrt{B^2 - 4AC}}{2A}, \\ A &= \beta, \\ B &= \beta + 1 - \gamma(T)^2, \\ C &= 1 - (\alpha + 1)(T)^2 + \alpha(T)^4,\end{aligned}\quad (18)$$

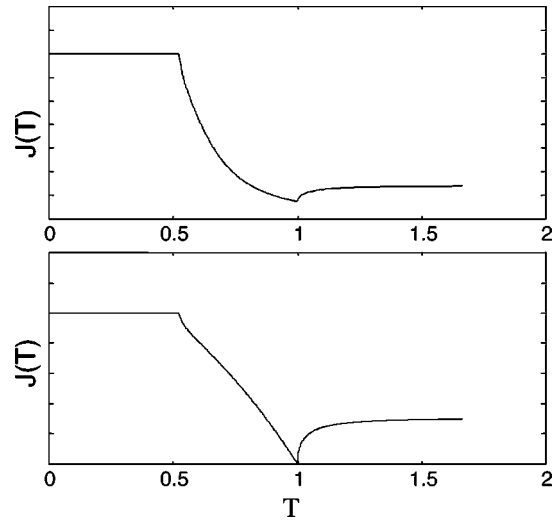


FIG. 4. Top: Theoretical displacement, u_3 , for the epicentral wave generated with a line source in Beryl as a function of T . Bottom: Theoretical displacement, u_3 , for the epicentral wave generated with a line source in an isotropic material (polycrystalline aluminum).

$$T = \frac{\tau}{x_3}.$$

Note that the definition for T has been redefined for the epicentral case (see Fig. 3 caption). Changing variables from ϖ to τ and operating on the expression for the vertical displacement, given in Eq. (16), with the inverse Laplace operator gives

$$\begin{aligned}u_3(0, x_3, T) &= \tilde{F}J(T), \\ J(T) &= \frac{1}{\pi F} \text{Re} \left\{ \bar{A}_3 \frac{\partial \varpi_1}{\partial \tau} H(T-1) \right. \\ &\quad \left. + \bar{A}_4 \frac{\partial \varpi_3}{\partial \tau} H(T-1/\sqrt{\alpha}) \right\}.\end{aligned}\quad (19)$$

A typical wave form generated from Eq. (19) using the material constants of Beryl is shown in Fig. 4. The displacement wave form for Beryl has characteristics similar to the displacement wave form for an isotropic material, also shown in Fig. 4. Both wave forms show the presence of two distinct wave arrivals.

2. Solution for class (ii) and (iii) materials

For class (ii) and (iii) materials, the Cagniard path no longer lies on the real ϖ axis. Before embarking on the solution for these materials, first the location of the branch points must be investigated. As was the case for solutions along $x_3=0$, branch points associated with $\zeta(\omega)$ may occur in two ways. In contrast to the surface wave case, the expression for \bar{u}_3 for the epicentral case is an odd function of $\sqrt{\phi(\varpi)}$, and as a consequence, the branch points arising from (i) need to be considered in addition to the branch points arising from (ii) [see Eq. (12)]. The expression for $\sqrt{\phi(\varpi)}$ may be rewritten as

$$\sqrt{\phi(\varpi)} = \sqrt{(\gamma^2 - 4\alpha\beta)(\varpi - \varpi_+)(\varpi - \varpi_-)},$$

$$\varpi_{\pm} = \frac{-[\gamma(\alpha+1) - 2\alpha(\beta+1)] \mp \sqrt{4[\alpha(\alpha+\beta-\gamma)(1+\alpha\beta-\gamma)]}}{(\gamma^2 - 4\alpha\beta)}.$$

Taking zinc as an example, ζ_1 will have branch points at $\varpi = \varpi_-$ and $\varpi = \varpi_+$ while ζ_3 will have branch points at $\varpi = \varpi_-$, $\varpi = \varpi_+$, $\varpi = -1$, and $\varpi = -1/\beta$. The Cagniard path for the first integral is again defined by Eq. (17), but ϖ is now a complex variable given by

$$\varpi = \varpi_1 + i\varpi_2. \quad (21)$$

Substituting Eq. (21) into Eq. (17), and equating the real and imaginary part of the equation gives

$$\gamma T^2 \varpi_1 + (\alpha+1)T^2 - \alpha T^4 = \beta(\varpi_1^2 - \varpi_2^2) + (\beta+1)\varpi_1 + 1,$$

$$\gamma T^2 \varpi_2 = 2\beta\varpi_1\varpi_2 + (\beta+1)\varpi_2. \quad (22)$$

The second equation of Eqs. (22) is satisfied if $\varpi_2 = 0$. Since the branch points for class (ii) and (iii) materials lie on the real axis, the first equation in Eqs. (22) imposes the additional constraints

$$\varpi_- \leq \varpi_1 \leq \varpi_+ \quad \text{for } \zeta_1(\varpi),$$

$$-1/\beta \leq \varpi_1 \leq \varpi_+ \quad \text{for } \zeta_3(\varpi). \quad (23)$$

If $\varpi_2 \neq 0$, then ϖ_2 and ϖ_1 can be expressed in terms of the parameter $T = \tau/x_3$ as follows:

$$\varpi_1(T) = \frac{\gamma T^2 - (\beta+1)}{2\beta}, \quad \varpi_2(T) = \frac{[\sqrt{4\alpha\beta - \gamma^2}(T^2 - T_-^2)(T^2 - T_+^2)]}{2\beta},$$

$$T_{\pm}^2 = \frac{-[\gamma(\beta+1) - 2\beta(\alpha+1)] \pm \sqrt{4\beta(\alpha+\beta-\gamma)(1+\alpha\beta-\gamma)}}{(4\alpha\beta - \gamma^2)}.$$

Using zinc as an example, the Cagniard paths for ζ_1 and ζ_2 are shown in Fig. 5. The expression for the out-of-plane displacement in Eq. (16) may be rewritten as

$$\bar{u}_3(0, x_3, \tau) = L^{-1} \left[\frac{1}{\pi} \text{Re} \left\{ \int_{\tau_0}^{\tau_+} I_{11} + \int_{\Gamma_1} I_{11} + \int_{\Gamma_2} I_{11} + \int_{\tau_0}^{\tau_e} I_{33} \right. \right. \\ \left. \left. + \oint_{\varpi_+} I_{33} + \int_{\tau_e}^{\tau_0} I_{33} \int_{\tau_0}^{\tau_+} I_{33} + \int_{\Gamma_3} I_{33} \right. \right. \\ \left. \left. + \int_{\Gamma_4} I_{33} \right\} \right],$$

$$I_{11} = \bar{A}_3 e^{-s\tau} \frac{\partial \varpi}{\partial \tau} d\tau, \quad I_{33} = \bar{A}_4 e^{-s\tau} \frac{\partial \varpi}{\partial \tau} d\tau,$$

$$\tau_0 = T_0 x_3 = \sqrt{\frac{(\alpha+1) - \sqrt{(\alpha+1)^2 - 4\alpha}}{2}},$$

$$\tau_e = T_e x_3 = \sqrt{\frac{-B + \sqrt{B^2 - 4\alpha C}}{2\alpha}}, \quad (25)$$

$$B = -(\varpi_+ \gamma + \alpha + 1),$$

$$C = \varpi_+^2 \beta + \varpi_+ (\beta + 1) + 1.$$

A plot of the theoretical displacement along the epicentral axis for zinc is given in the inset of Fig. 6. The character of the epicentral wave form for zinc is considerably different than its isotropic counterpart, shown in Fig. 4. The arrivals of

the various wave fronts in Fig. 6 is best understood by referencing the portion of the wave front curve that pierces the symmetry axis, Fig. 5 inset. The first wave arrival corresponds to the longitudinal branch of the wave front curve. The solution gives zero for the portion of the wave that corresponds to the interior of the cuspidal triangle. This zone behind the leading wave front is referred to as a lacuna. The solution has a singularity at $T = T_+$ corresponding to the conical point on the wave front.

C. Observation points off the symmetry axis

Consider the inverse of Eq. (5) for observation points that are neither along the symmetry axis nor on the bounding surface. The geometry of the problem is shown in Fig. 1 where now the point of observation is point C. The source is a surface line source. The observation angle, θ , is defined as the angle between the symmetry axis and a line joining the source and observation point. Formally, the inverse of Eq. (5) is written as

$$\bar{u}_3(x_2, x_3, \tau) = L^{-1} \left[\frac{1}{\pi} \text{Re} \int_0^\infty (A_3 e^{-\zeta_1 x_3 s} \right. \\ \left. + A_4 e^{-\zeta_3 x_3 s}) e^{is\omega|x_2|s} ds \right]. \quad (26)$$

The Cagniard path for Eq. (26) is defined by

$$(a) \quad \zeta_1 x_3 - i\omega|x_2| = \tau,$$

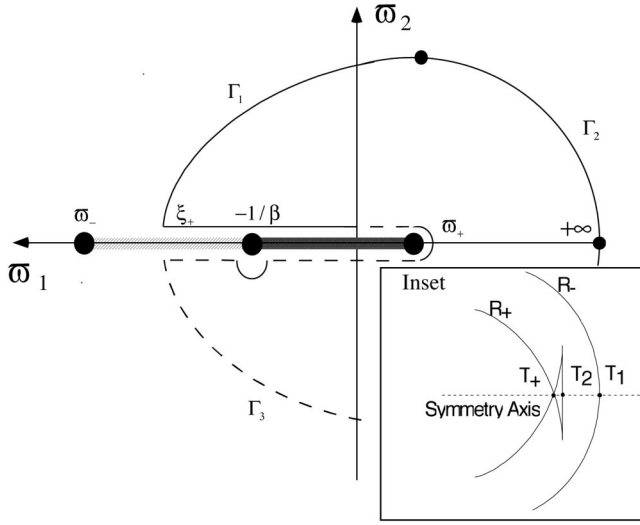


FIG. 5. Cagniard contour for zinc for observation points along the symmetry axis. Solid line represents contour corresponding to ζ_1 and the dashed line represents the contour corresponding to ζ_3 . Inset: Enlargement of wave front near symmetry axis.

$$(b) \quad \zeta_3 x_3 - i\omega |x_2| = \tau, \quad (27)$$

τ is real and positive.

The parametric equations representing the Cagniard path are obtained by substituting Eqs. (8) into Eqs. (27) and squaring twice to eliminate the radicals. This procedure yields a fourth order equation for ω of the form

$$A(\theta)\omega^4 + B(\theta, T)\omega^3 + C(\theta, T)\omega^2 + D(\theta, T)\omega + E(\theta, T) = 0,$$

$$A(\theta) = F(\theta) + 4\alpha\beta - \gamma^2,$$

$$B(\theta, T) = \frac{8i\alpha T \sin(\theta)F(\theta)}{\cos^2(\theta)},$$

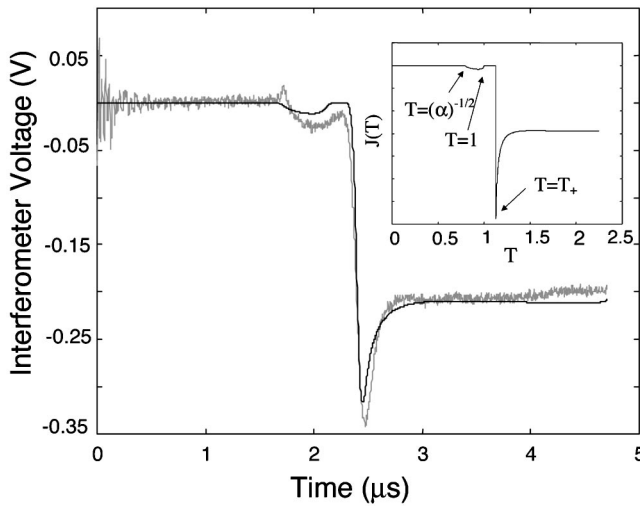


FIG. 6. Comparison between experiment and theory for the epicentral case. The sample is single crystal zinc with the c axis perpendicular to the free surface. The nonzero experimental displacement corresponding to the interior of the cuspidal triangle is a result of pulse broadening. Inset: Theoretical displacement, u_3 , for the epicentral wave generated with a line source in zinc as a function of T .

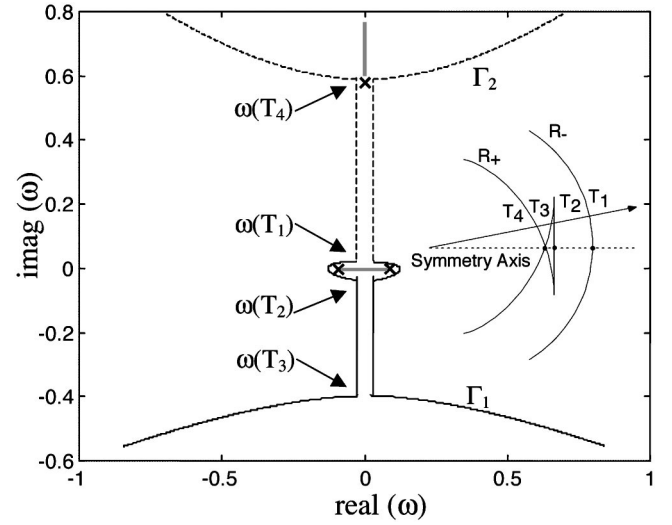


FIG. 7. Cagniard contour for zinc for observation points off the symmetry axis ($\theta = 10^\circ$). Solid line represents contour corresponding to Eq. (27a) and the dashed line represents the contour corresponding to Eq. (27b). Inset: Enlargement of wave front near symmetry axis.

$$C(\theta, T) = 2F(\theta)G(\theta, T) - 16 \frac{\alpha^2 T^2 \sin^2(\theta)}{\cos^4(\theta)} - 2(\alpha + 1)\gamma + 4\alpha(\beta + 1), \quad (28)$$

$$D(\theta, T) = \frac{8i\alpha T \sin(\theta)G(\theta, T)}{\cos^2(\theta)},$$

$$E(\theta, T) = G(\theta, T) - (\alpha + 1)^2 + 4\alpha,$$

$$F(\theta) = - \left(\frac{2\alpha \sin^2(\theta) + \gamma \cos^2(\theta)}{\cos^2(\theta)} \right)^2,$$

$$G(\theta, T) = \frac{2\alpha T^2 - (1 + \alpha)\cos^2(\theta)}{\cos^2(\theta)}.$$

Equation (28) has four complex roots, Θ_1 , Θ_2 , Θ_3 , and Θ_4 , which occur in complex conjugate pairs. The roots labeled Θ_1 and Θ_3 correspond to the physical sheets of the Riemann surface. For the special case of an isotropic solid, $\alpha = \beta = \gamma/2$, Eq. (28) can be factored into two second order equations that can be solved analytically. For the present problem of transverse isotropy, the roots must be found numerically.

The character of the Cagniard paths is dictated by the location of the lacunas relative to the observation direction. Thus, all crystal classes will have Cagniard paths with similar characteristics. As a representative example, the Cagniard path for zinc will be discussed in detail. The wave front for zinc is shown in the inset of Fig. 7. The lacunas in the R_+ branch are centered along the symmetry axis and along the bounding surface. Figure 7 shows the Cagniard path for an observation angle, $\theta = 10^\circ$, that intersects the lacuna. With the Cagniard path numerically defined, the inversion of the transformed displacements, Eq. (26), may be performed. The off epicentral vertical displacement in zinc for a detection angle of 10° is shown in the inset of Fig. 8. The characteris-

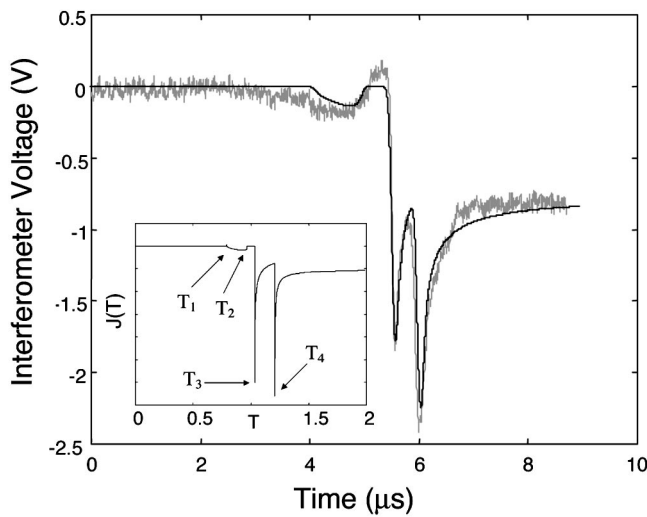


FIG. 8. Comparison between experiment and theory for an observation point off the symmetry axis. The sample is single crystal zinc with the c axis perpendicular to the free surface ($\theta=10^\circ$). Inset: Theoretical out-of-plane displacement due to line-source excitation in zinc as a function of T .

tics of the wave form shown in Fig. 8 are similar to the epicentral wave form shown in Fig. 6. The primary difference is the splitting of the wave resulting corresponding to the conical portion of the wave front.

III. EXPERIMENT

The experimental setup used to generate and detect ultrasound is shown in Fig. 9. The generation of the ultrasonic disturbance was accomplished by irradiating the sample with a pulsed Nd:YAG operating at $1.064\ \mu\text{m}$.²⁶⁻²⁸ The transverse spatial profile was Gaussian and the temporal pulse length was approximately 10 ns. The energy per pulse was typically 20 mJ. The ultrasonic disturbance was detected with a skew-stabilized Michelson interferometer operating at 632.8 nm. The upper limit of the bandwidth was determined to a large extent by the frequency response of the photodetectors in the interferometer. The photodetectors were manufactured by EG&G (product designation FFD-040) and have a specified upper bandwidth limit of 150 MHz into a $50\ \Omega$ load. The lower limit of the bandwidth, estimated at 1 kHz, was dic-

tated by the characteristics of the stabilization circuit. If the interferometer signal voltage is much smaller than the interferometer peak-to-peak voltage, then the signal voltage and the surface displacement are related as follows:

$$D_s = V_i \left(\frac{632.8\ \text{nm}}{2\pi} \right), \quad (29)$$

where D_s represents the surface displacement and V_i represents the ratio of the interferometer signal voltage to the peak to peak voltage.

For same side detection, care had to be taken so as not to saturate the photodiodes in the interferometer with light from the Nd:YAG laser that had scattered off the sample surface. A beam stop was used to collect the specular component of the scattered light while a $1.064\ \mu\text{m}$ band reject filter was used to block the remaining scattered light from reaching the photodiodes. In order to approximate an infinite line source, a convex/concave lens combination was used as a telescope to expand the beam while a cylindrical lens was used to focus the generation beam to a line. This technique of generating a laser line source was exploited by Aindow *et al.*²⁹ to produce high amplitude surface acoustic waves. The approximate line dimensions, as measured from a piece of laser profiling paper, were $20\ \text{mm} \times 0.2\ \text{mm}$.

The single crystal zinc specimens were cleaved along basal planes and then polished using Buehler Carbimet paper to produce a mirrorlike surface. The crystal orientation was determined using x-ray diffraction. The polished surface was perpendicular to the x-ray beam resulting in a diffraction pattern that had sixfold symmetry, confirming that the polished surface coincided with the basal plane. The cylindrical zinc sample used for same side detection had a radius of 15 mm and a length of 60 mm. The sample used for detection of epicentral waves had a radius of 15 mm and a length of 5 mm. The voltage signals from the interferometer were recorded using a LeCroy 9354m digital oscilloscope operating at 500 M samples/s.

IV. RESULTS AND DISCUSSION

A comparison between theory and experiment for same side detection is presented for single crystal zinc (c axis perpendicular to the surface) in Fig. 3. The experimental curve is single shot data and the source/receiver separation was 9.1 mm. The theoretical result, inset Fig. 3, is convolved with a Gaussian function (full width at half-maximum=300 ns) in order to mimic broadening effects. Pulse broadening for same-side detection is mainly caused by the finite transit time of the acoustic signal across the detection/generation spot. The first disturbance turns on and off at times corresponding to the arrival of the longitudinal wave and shear wave, respectively. The largest disturbance corresponds to the Rayleigh pole and is in the form of a traveling delta function. The amplitude of the Rayleigh wave for the theoretical curve was scaled to match the experimental amplitude. Since the data was single shot, comparison of theoretical and experimental amplitudes allows an estimate of the optical reflection coefficient. The theoretical amplitude, given in Eq. (18), is expressed by

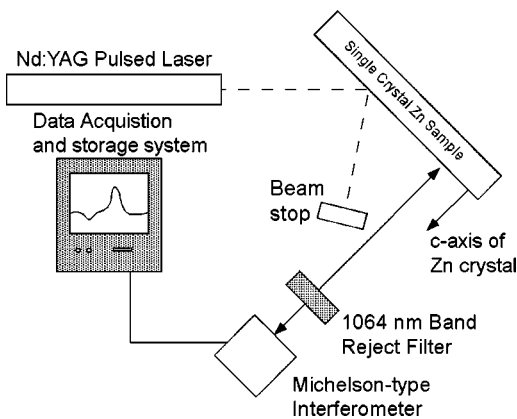


FIG. 9. Experimental setup. A Nd:YAG laser is used to generate the ultrasonic disturbance and a Michelson-type interferometer is used to detect the ultrasound.

$$A_{\text{Rayleigh}} = \bar{F} \psi_r q_0 \left(\frac{1}{\bar{N} \sqrt{\pi}} \right) \sqrt{C_{44}/\rho},$$

$$\bar{F} = \frac{1}{\rho C} \left[\frac{B_{33}}{C_{44}} (1 - \kappa) + \frac{B_{22}}{C_{44}} \alpha \right], \quad (30)$$

where q_0 represents the absorbed laser energy and \bar{N} represents the Gaussian pulse width. The data shown in Fig. 3 was produced by a 37 mJ pulse distributed over 1 cm. Scaling the theoretical amplitude of the Rayleigh wave to match the experimental data, the reflectivity at the sample surface was estimated to be 90%, which is comparable to published values for zinc. It should be noted that the accuracy of these results decreases as the aspect ratio, the ratio between the line source length and the source receiver distance, decreases.

Before comparing experiment and theory for the epicentral and off-epicentral cases, the effect of ultrasonic reflections from the back surface of the sample must be considered. Each time the wave reflects off the sample surface, the amplitude and temporal character of the wave are modified. The modification to the wave is described by reflection coefficients, which are a function of observation angle. For the isotropic case, Rose¹⁷ shows that along the epicentral direction, reflection primarily alters the amplitude of the reflected wave. It is assumed that a similar result holds for anisotropic materials and for small angles off axis. Since the emphasis in this paper is to compare the temporal character between experiment and theory, the effect of reflection off the back surface will not be taken into account.

Figure 6 compares theory and experiment for displacement along the epicentral axis for a sample of single crystal zinc (c axis perpendicular to the free surface). The source/receiver distance was 5 mm and the signal was averaged 25 times to improve the signal-to-noise ratio. Again, the theoretical result was convolved with a Gaussian (FWHM=20 ns). Pulse broadening for detection along the epicentral direction is primarily due to the finite temporal pulse width of the generation laser. Zinc is a class (iii) crystal and, as a result, the displacement character differs markedly from its isotropic counterpart, Fig. 4. In a fashion similar to that of the surface wave case, the first disturbance turns on and off at times corresponding to the arrival of the longitudinal wave, T_1 , and shear wave, T_2 , respectively. After T_2 , the displacement is identically zero until the arrival of the majority of the acoustic energy at T_+ . A comparison between experiment and theory for an observation point off the symmetry axis, $\theta=10^\circ$, is shown in Fig. 8. Similar to the analysis presented in Fig. 6, the data was averaged 25 times and convolved with a Gaussian ($\bar{N}=20$ ns). Figure 8 clearly shows the splitting of the wave caused by the conical portion of the wave front.

V. CONCLUSION

It was found that for a transversely isotropic half-space, the laser source could be modeled as a shear stress dipole applied at the free surface. A formal solution of the problem was found using double (Fourier–Laplace) transforms. The

Cagniard–de Hoop technique was used to analytically invert the transformed solution for the epicentral case as well as for the surface wave case. A quasianalytical approach, where the Cagniard path was defined numerically, was used to invert the transformed solution for observation points off the symmetry axis.

Experimental validation of the theory was performed using single crystal zinc samples. The zinc samples were cut to have the free surface coincide with a plane of isotropy. Theoretical and experimental results for zinc agreed well for all the source/observation geometries considered.

ACKNOWLEDGMENTS

The authors gratefully acknowledge Dr. Robert E. Green for helpful suggestions regarding the experimental procedure and for supplying single crystal zinc samples. This work was sponsored by the U.S. Department of Energy, Office of Science-BES, Materials and Engineering Physics program under DOE Idaho Operations Office Contract No. DE-AC07-99ID13727.

- ¹C. Scruby, R. Dewhurst, D. Hutchins, and S. Palmer, "Laser generation of ultrasound in metals," *Research Techniques in Nondestructive Testing* (Academic, New York, 1982), Vol. 5, pp. 281–327.
- ²C. Scruby, R. Smith, and B. Moss, "Microstructural monitoring by laser-ultrasound attenuation and forward scattering," *NDT Int.* **19**, 307–313 (1986).
- ³K. Telschow, "Microstructural characterization with a pulsed laser ultrasonic source," *Review of Progress in Quantitative Nondestructive Evaluation* (Plenum, New York, 1988), Vol. 7b, pp. 1211–1218.
- ⁴E. P. Papadakis, "Scattering in polycrystalline media," *Methods Exp. Phys.* **19**, 237–298 (1981).
- ⁵M. J. P. Musgrave, *Crystal Acoustics* (Holden-Day, Inc., San Francisco, 1970).
- ⁶R. Stoneley, *Proc. R. Soc. London, Ser. A* **232**, 447–458 (1955).
- ⁷D. Royer and E. Dieulesaint, "Rayleigh wave velocity and displacement in orthorhombic, tetragonal, hexagonal, and cubic crystals," *J. Acoust. Soc. Am.* **76**, 1438–1444 (1984).
- ⁸E. A. Kraut, *Rev. Geophys.* **1**, 401 (1963).
- ⁹H. Lamb, *Philos. Trans. R. Soc. London, Ser. A* **203**, 1 (1904).
- ¹⁰L. Cagniard, *Reflection and Refraction of Progressive Seismic Waves* (McGraw-Hill, New York, 1962).
- ¹¹A. T. de Hoop, *Appl. Sci. Res., Sect. B* **8**, 349 (1960).
- ¹²R. Burridge, "Lamb's problem for an anisotropic half-space," *Q. J. Mech. Appl. Math.* **24**, 81–98 (1970).
- ¹³J. R. Willis and R. J. Bedding, "Arrivals associated with a class of self-similar problems in elastodynamics," *Math. Proc. Cambridge Philos. Soc.* **77**, 591–607 (1975).
- ¹⁴A. Mourad, M. Deschamps, and B. Castagnède, "Acoustic waves generated by a transient line source in an anisotropic half-space," *Acust. Acta Acust.* **82**, 839–851 (1996).
- ¹⁵R. L. Weaver, W. Sachse, and K. Y. Kim, "Transient elastic waves in a transversely isotropic plate," *J. Appl. Mech.* **63**, 337–346 (1996).
- ¹⁶C. B. Scruby, R. J. Dewhurst, D. A. Hutchins, and S. B. Palmer, "Quantitative studies of thermally generated elastic waves in laser-irradiated metals," *J. Appl. Phys.* **51**, 6210–6216 (1980).
- ¹⁷L. R. F. Rose, "Point source representation for laser generated ultrasound," *J. Acoust. Soc. Am.* **75**, 723–732 (1984).
- ¹⁸D. H. Hurley, "Laser-generated thermoelastic sources in anisotropic materials," *J. Acoust. Soc. Am.* **115**, 2054–2058 (2004).
- ¹⁹R. G. Payton, *Elastic Wave Propagation in Transversely Isotropic Media* (Martinus Nijhoff, The Hague, 1983).
- ²⁰E. A. Kraut, Ph.D. thesis, University of California, Los Angeles, 1962.
- ²¹D. H. Hurley and J. B. Spicer, "Point-source representation for laser-generated ultrasound in an elastic, transversely isotropic half space," *J. Appl. Phys.* **86**, 3423–3427 (1999).
- ²²In Ref. 21 it was shown that the vertical displacement along the epicentral

direction for a point source can be obtained by taking a temporal and spatial derivative of the line source solution.

²³The effect of heat diffusion has been neglected and q_0 represents the laser energy absorbed by the sample. Rose (Ref. 17), states that a point-source representation for the radiation from a localized source is adequate for $\lambda \gg h$ where λ is the ultrasonic wavelength and h is the largest characteristic length relating to the source region. Ready (Ref. 24) has shown that the source is effectively localized within a region, $0 \leq h \leq \omega + (4kt)^{1/2}$, where ω is the laser beam radius and t is the time interval of interest. Considering laser generation in zinc, it can be shown that for a spot size of $10 \mu\text{m}$, it is reasonable to neglect the effects of thermal diffusion for frequencies below 100 MHz.

²⁴J. F. Ready, *Effects of High-Powered Laser Radiation* (Academic, New York, 1971).

²⁵The solution procedure involves applying a Fourier/Laplace transform to remove dependence on the spatial and temporal variables: $F(\eta, s) = \int_{-\infty}^{\infty} \int_0^{\infty} f(x_2, t) e^{-(i\eta x_2 + s\tau)} d\tau dx_2$.

²⁶S. J. Davies, C. Edwards, G. S. Taylor, and S. B. Palmer, "Laser-generated ultrasound: Its properties, mechanisms and multifarious applications," J. Phys. D **26**, 329–348 (1982).

²⁷R. J. Dewhurst, C. Edwards, A. D. W. Mckie, and S. B. Palmer, "Comparative study of wide-band ultrasonic transducers," Ultrasonics **25**, 315–321 (1987).

²⁸D. A. Hutchins, "Mechanisms of pulsed photoacoustic generation," Can. J. Phys. **64**, 1247–1264 (1986).

²⁹A. M. Aindow, R. J. Dewhurst, and S. B. Palmer, "Laser-generation of directional surface acoustic waves pulses in metals," Opt. Commun. **42**, 116–120 (1982).